RESEARCH ARTICLE

High-speed observation of dynamic delamination failure in tapered composite laminates under tensile loading

Mirac Onur Bozkurt[1,2] | **Emine Burcin Ozen**[1] | **Burak Ogun Yavuz**[1] | **Levend Parnas**[3] | **Demirkan Coker**[1,2]

[1]Department of Aerospace Engineering, Middle East Technical University, Ankara, Turkey

[2]METU Center for Wind Energy, Middle East Technical University, Ankara, Turkey

[3]Department of Mechanical Engineering, TED University, Ankara, Turkey

Correspondence
Demirkan Coker, Department of Aerospace Engineering, Middle East Technical University, Ankara 06800, Turkey.
Email: coker@metu.edu.tr

Present addresses
Mirac Onur Bozkurt, Imperial College London, London, UK; Emine Burcin Ozen, University of Oxford, Oxford, UK; and Burak Ogun Yavuz, University of Bristol, Bristol, UK.

Abstract

This article presents high-fidelity observations of the time evolution of unstable delamination growth in tapered composite beams under tensile loading via ultra-high-speed camera in conjunction with digital image correlation. Asymmetrically tapered GFRP laminates, with a thickness drop from 18 plies to 12 plies, are manufactured in three different layup configurations with grouped drop-offs: $[0_6/(0_2)_3/0_6]$, $[0_6/\underline{0_6}/0_6]$, and $[0_6/(\pm45)_3/0_6]$. Beam specimens are subjected to quasi-static tensile loading in a servo-hydraulic axial testing machine, and the damage evolution on one edge of the tapered beam is monitored in situ at 124,000 fps with a high-speed camera (HSC). In selected tests, digital image correlation (DIC) analyses are conducted either on the edge or on the tapered surface to obtain the full-field strain and elucidate failure mechanisms. Real-time HSC observations of the damage sequence consistently affirm that the initial failure mechanism is a transverse crack at the nearest drop-off to the thin section, which is followed by delaminations at interfaces of sublaminates. Unstable delamination growth is characterized by measurements of lower bounds of crack tip speeds. The unique crack speed data provide evidence for the existing effect of through-the-thickness stresses on delamination growth. The detailed sequence and patterns of dynamic failure presented in this paper can serve as a benchmark to validate damage models used in simulations of tapered laminates.

Highlights

- The sequence of unstable delamination growth in tapered GFRP beams is investigated experimentally.
- Characterized unstable delamination growth based on crack tip speed measurements.
- Strain fields are evaluated along beam edges using DIC in real-time.
- In-situ observations of dynamic failure can serve as a benchmark to validate damage models.

1 | INTRODUCTION

Tapered composite laminates are widely used in the design of helicopter rotors where various degrees of flexibility are required to satisfy several structural requirements under complex dynamic characteristics. The tapered geometry of such structures is achieved by dropping off composite plies at different locations along the laminate. However, material and geometry discontinuities induced by these drop-offs often act as sources of large interlaminar stresses, leading to delamination and ultimately premature failure.[1] Therefore, understanding failure mechanisms in tapered composites is crucial for the design of robust and reliable structural components.

Failure mechanisms in tapered laminates have been investigated based on experimental observations on simpler laminate configurations. In one of the earliest studies, Hoa et al.[2] reported that delamination failure in symmetrically tapered glass/epoxy and graphite epoxy beams occurs with no sign in the stress–strain response under tension. Curry et al.,[3] who conducted static tensile tests on asymmetric graphite/epoxy tapered specimens with grouped drop plies, identified the first major failure as a delamination at the belt-core interface by taking photographs of their specimens just after the failure. Fish and Lee,[4] who investigated the tensile and compression failure characteristics of symmetrically tapered glass/epoxy beams, also observed that delamination was the common failure mode for different tapered laminate configurations. They reported that delamination was detectable through audible indications as well as a large load drop, but its growth was unstable initially. Fish and Vizzini[5] examined tensile failure of unidirectional tapered laminates with different drop-off configurations. They reported stable delamination growth in laminate configurations with dispersed drop-offs while they observed unstable delamination growth in laminates with grouped drop-offs and connected resin pockets.

Given the variability of experimental observations on different laminate configurations, parametric and analytical approaches, such as stress analysis and prediction of failure loci, have become of great interest to achieve better understanding of failure mechanisms in the absence of real-time observations. Several researchers have taken a combined analytical/experimental approach to investigate the effect of different parameters on the failure of tapered laminates, for example, step spacing,[6] number and angle of plies grouped together,[7] geometrical asymmetry,[8] taper angle.[9] Wisnom[10] identified the critical factor controlling the delamination as the strain energy release rate associated with ply drop-offs. He proposed a simple fracture energy-based delamination prediction criterion to use as a basis for the design of tapered laminates. Several other studies have also focused on developing simplified energy-based approaches to predict ply-drop delamination.[11,12] A few design guidelines for tapered laminates were developed by Mukherjee and Varughese[13] following a parametric study through a set of global–local finite element simulations.[14]

In the lack of in-situ real-time experimental evidence, understanding of the damage process in laminates with discontinuities has been limited to numerical simulations and post-mortem experimental observations. Only a few studies attempted to observe the initial failure sequence real-time. In a recent study, Zhang et al.[15] performed an experimental investigation to characterize the tensile failure mechanisms of tapered laminates as the basis for their high-fidelity modeling efforts. They tested modestly and severely tapered laminate configurations of design-level complexity where they were able to capture the failure sequence in modestly tapered specimens. They could not identify the initial failure mechanism in severely tapered laminates, as the failure events were intricate and highly dynamic, and besides, it can be deduced that their severely tapered configuration was too complex when compared to the resolution of high-speed photographs. Gordon et al.[16] also included a high-speed camera (HSC) in their experimental setup for tensile testing of tapered beams with conventional and scarf plies. They captured delamination onset in several successive frames; however, they were not able to identify delamination initiation sites due to the dynamic nature of the failure process.

In this study, we experimentally investigate the failure process in staircased-grouped type asymmetrically tapered glass fiber reinforced polymer (GFRP) laminates under static tensile loading. We present high-fidelity observations of the time evolution of the unstable delamination growth in tapered composite beams under tensile loading via ultrahigh-speed camera in conjunction with digital image correlation. In situ real-time observations of the failure event are shown to be necessary to elucidate the failure sequence which consists of a resin crack associated with unstable delamination growth(s). To justify the failure mechanisms observed in high-speed camera frames, strain contours are obtained on the tapered face and edge of the beam through digital image correlation (DIC) analyses. It is shown that dynamic failure sequence differs between the laminates having 0° drop-off plies and ±45° drop-off plies.

2 | EXPERIMENTAL METHOD

2.1 | Specimen

Asymmetrically tapered composite specimens were manufactured from unidirectional GFRP prepregs by hand-layup technique. The prepregs with a nominal thickness of 0.244 mm are composed of HexPly 913 epoxy matrix reinforced with S2 glass fibers. Mechanical and interface properties of the HexPly S2-Glass/913 UD prepregs are given in Table 1.

Laminates with discontinuous plies were laid on a flat mold assuring that one face of the beam is constrained to be flat, and inherently, the other face is tapered. The use of flat mold offers several advantages such as precise flatness of the base and dropped layers and smooth transition along the tapered region which decreases stress concentrations due to geometry-induced corners. On the other hand, modeling such a smooth transition may not be straightforward. To achieve an enhanced dimensional accuracy at layer positioning, two rulers were located to each side of the molding surface. During the hand lay-up process, compaction was applied upon laying of every four layers. Additional tab material (S2-glass woven fabric stacked in $\pm45°$ orientations) with 50 mm length were laid on the tapered side at both ends of the laminate to

TABLE 1 Mechanical properties of GFRP material.

Density	1850 kg/m³
Cured ply thickness	0.244 mm
Fiber volume fraction	0.51
Elastic	$E_{11} = 50$ GPa, $E_{22} = 12$ GPa $\nu_{12} = 0.3$, $G_{12} = 4$ GPa
Ply strength	$X_T = 1400$ MPa, $X_C = 1100$ MPa $Y_T = 50$ MPa, $Y_C = 200$ MPa, $S_L = 90$ MPa
Interface strength	$T_{o,I} = 46$ MPa, $T_{o,II} = 71$ MPa
Fracture toughness	$G_{Ic} = 1250$ N/m, $G_{IIc} = 1248$ N/m

obtain equal grip thicknesses. Following the lamination, autoclave curing was conducted at 80°C for 30 min and 120°C for 60 min at 4-bars pressure. Flat specimen tabs which were manufactured separately were bonded to the flat side of the laminate. Manufactured tapered laminates were cut into 209×25 mm beams by a CNC grinding cutter. To eliminate possible premature crack nucleation from any cutting-induced flaw on the side surfaces, specimens were ground and polished with 400-to-4000 grit SiC papers. In addition to alleviating the roughness, the polishing enables better in-situ and post-mortem visualization of the side surfaces as well as the early diagnosis of any defects which might have been induced by manufacturing processes. No defects were detected in the micrographic examination of the specimens prior to testing.

The geometry of the asymmetrically tapered specimen is shown in Figure 1. Tapered specimens are configured such that the thick and thin sections of beams consist of 18 and 12 plies, respectively. These ply numbers correspond to 4.39 and 2.93 mm nominal thicknesses. To satisfy a nominal taper angle of 9.5°, the length of the tapered section is chosen as 9 mm.

In this study, dynamic delamination in tapered beams was investigated through laminates with grouped drop-off plies, as dispersed configurations are likely to have the characteristic of slow delamination growth.[5] Staircased-grouped tapered specimens with three different configurations were manufactured with different stacking combinations of 0°, +45°, and −45° layers, as illustrated in Figure 2. Two unidirectional configurations (A) and (B) have discontinuous 0° plies which were cut at three and six consecutive steps, respectively, while the configuration (C) have discontinuous +45°/−45° plies which were cut at three consecutive steps.

2.2 | Experimental setup

Static tensile tests of asymmetrically tapered beams have been conducted in a 250 kN MTS universal servo-
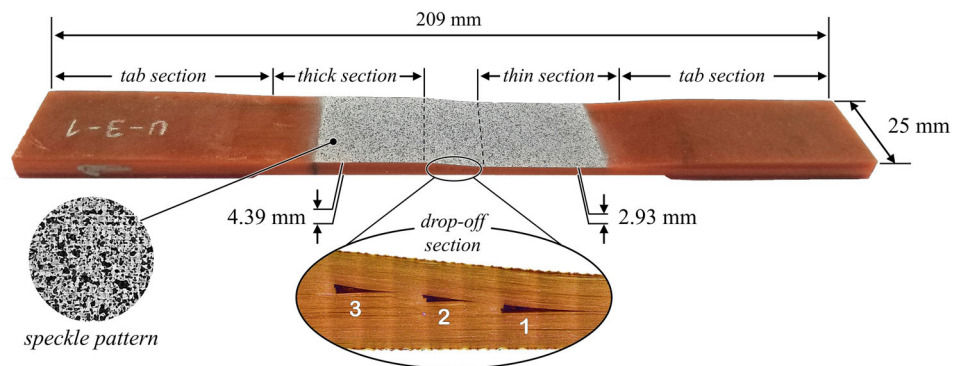

FIGURE 1 Dimensions and close-up views of the asymmetrically tapered test specimen with numbering of resin pockets.
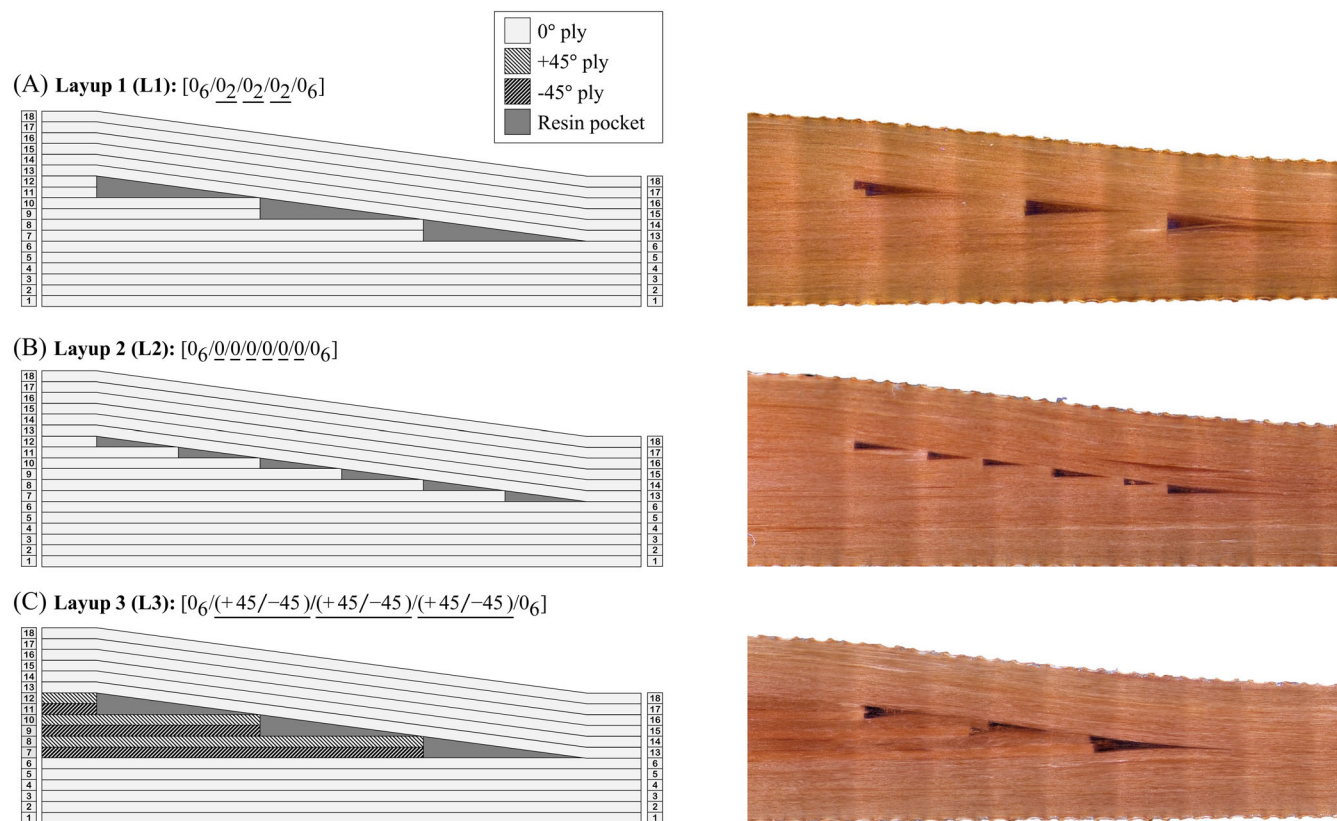
FIGURE 2 Laminate configurations (left) and side views of manufactured specimens (right). Underlined angles indicate drop-off plies.

hydraulic testing machine seen in Figure 3. Thin and thick sections of the specimens were positioned inside the upper and lower hydraulic wedge grips, respectively, such that the free span length is 109 mm and equal portions of 50 mm remained inside each grip. Throughout the experimental program, grip pressures between 20 and 25 MPa were applied to squeeze specimens to prevent sliding inside the grips. All tensile tests were carried out in displacement control mode with a stroke rate of 0.5 mm/min, and the displacement was applied through the vertical motion of the lower grip while the upper grip was fixed.

In order to capture the damage sequence in a possible dynamic failure scenario, the high-speed photography technique was used. During each test, the specimen was lit by two Dedocool COOLH lights with 250 W Osram HLX Tungsten lamps. Failure events were recorded from the edge by a Photron SA5 ultra-high-speed camera at 124,000 fps providing images of 128 × 288 pixels resolution. To acquire the above-mentioned settings, the ultra-high-speed camera was equipped with a Titanar lens having 5.6-to-100 mm focal length and a 150 mm distance ring. The recording was triggered manually following a loud sound indicating failure or a sudden load drop in the real-time load–displacement curve. In some tests, snapshots were also taken at every 10 s during the loading not to miss any stable damage formation and

progression. After each experiment, the resultant damage on the beam edge was characterized by Huvitz HDS-5800 digital microscope.

In the experiments of selected specimens, DIC analyses were conducted for two purposes: (i) on the tapered surface, to measure the deformation and strain along the beam, and (ii) on the edge, to observe the strain concentrations at the tapered region. In the case of DIC on the tapered surface, experiment was recorded at a rate of 1 Hz via a 1 MP camera seen in Figure 3 with a resolution of 1024 × 1024 pixels. In the case of DIC analyses on the specimen edge, snapshots taken by the HSC were used. All analyses were conducted using NCORR which is an open DIC tool developed in the MATLAB environment.[17] In the calculations, the subset radius was set to 20 pixels with a travel size of 5 pixels. The radius used in strain computations was set to 15 pixels.

As a result of the high effective moduli and moderate effective thicknesses of test coupons, stiffnesses of the tapered beams are quite high and comparable with that of the testing machine to a certain degree. Therefore, stroke data taken from the testing machine are not expected to represent only the elongation of a specimen but also involves an additional displacement due to the machine compliance. In such cases, real deformation fields obtained from the DIC analysis can be used to eliminate

FIGURE 3 Experimental setup for the observation of a dynamic failure sequence in tapered laminates under tensile loading.
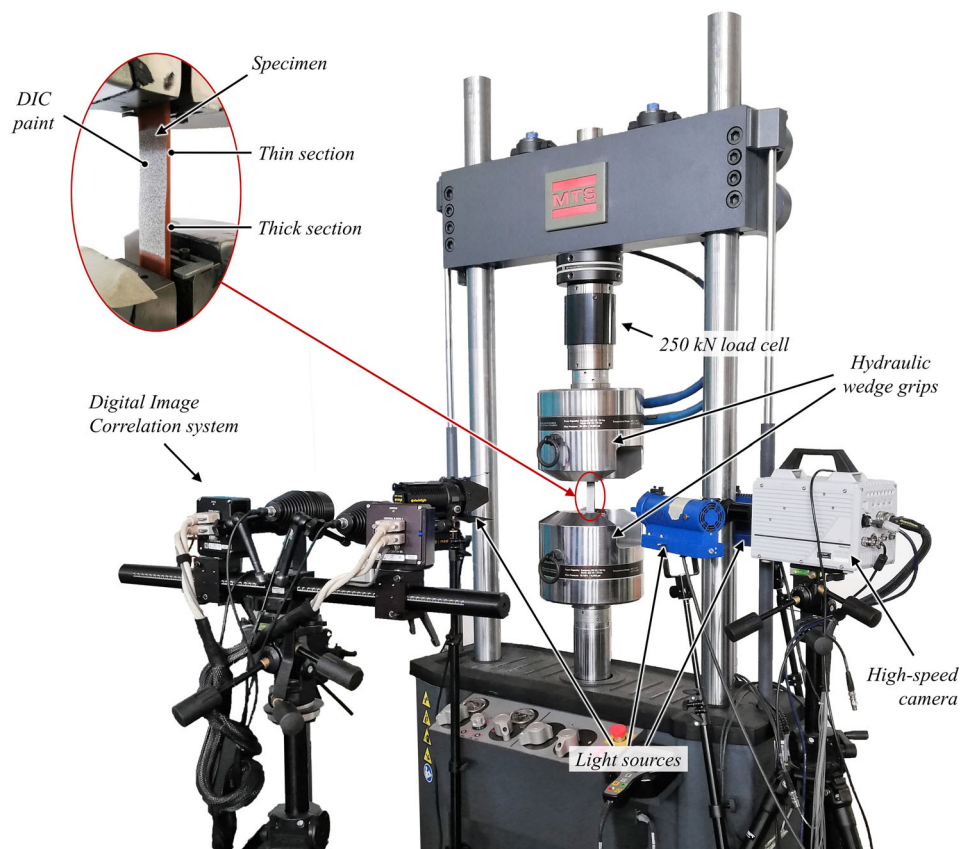
the latter addition from the raw stroke data. Accordingly, we characterized the amount of stroke induced by the machine compliance via a DIC analysis on the tapered surface. In all tensile tests, the corresponding partial amount of stroke induced by the test machine has been subtracted from the overall stroke measurement to obtain the actual axial deformation of tested specimens.

3 | EXPERIMENTAL RESULTS AND DISCUSSION

3.1 | Overall force-elongation responses

Effective stress, σ_{eff}, vs elongation curves obtained from tensile tests of four asymmetrically tapered specimens are presented in Figure 4, where $\sigma_{\text{eff}} = load/(width \times t_{\text{eff}})$ and $t_{\text{eff}} = 2(t_{\text{thick}} t_{\text{thin}})/(t_{\text{thick}} + t_{\text{thin}})$. Unidirectional configurations L1 and L2 show very similar mechanical responses in terms of their stiffnesses and the effective stresses at failure. The stiffness of L3 configuration, however, is slightly lower but its failure stress is significantly higher compared to that of the other two configurations. Load, effective stress, and elongation measurements recorded just before the failure and percentage load drops in all specimens are reported in Table 2. In addition to its greater failure load and elongation values, L3

configuration loses only 0.7% of its tensile load carrying capacity upon failure. In the case of unidirectional laminates, that is, L1 and L2 configurations, percentage load drops are relatively higher, being around 12%–15%.

In the case of L1 specimens, undamaged portions of two curves are almost identical ensuring the specimen quality and reproducibility of tests. The non-linearity of the force–stroke curves is attributed to the frictional sliding, the existence of which is confirmed after the tests by the directional traces formed on tab surfaces. A load drop occurs in both tests at close tensile stress and elongation values which are recorded as (1.33%, 547.6 MPa) and (1.38%, 563.3 MPa) for L1-1 and L1-2, respectively. Furthermore, the loss in load carrying capacity is measured to be 12% for both specimens. In the following sections, mechanisms leading to these failure characteristics are examined for each specimen through the real-time observation of the failure and the DIC analysis.

3.2 | Results of L1 configuration

Load drops observed in the force–stroke curves of L1 specimens are due to an unstable delamination growth that initiates inside the tapered region. Figure 5 presents the HSC images showing the sequence of such dynamic failure in L1-1 with an interframe time of 8 µs. In these

images, the delaminations reveal themselves as white narrow regions and their tips are indicated by red arrows where possible. In the first frame captured by the HSC, two delaminations to the left are branched from a transverse crack at the vertical wall of the first resin pocket and propagate towards the thick end of the transition region. The upper delamination is at the interface of the belt (upper) and drop-off (middle) sublaminates, while the lower delamination is at the interface of the drop-off and core (lower) sublaminates. In addition, another transverse crack is noticeable next to the first one within the first resin pocket. In the next 47 HSC frames, which correspond to a time interval of 379 μs, no significant progression in the damage state is observed indicating that the delamination growth is stable or arrested during this interval. The stable growth of delaminations can be attributed to the existence of high through-the-thickness compressive stresses despite high interlaminar shear stresses in the vicinity of the top-left and bottom-left corners of the first resin pocket.[13]

In the next frame taken 8 μs later at 387 μs, two existing delaminations propagate unstably with lower bound average crack tip speeds of 389 and 585 m/s for the upper and lower delaminations, respectively. (We call these speeds "lower bound," because an interframe time of 8.1 μs is used in the speed calculations. Howev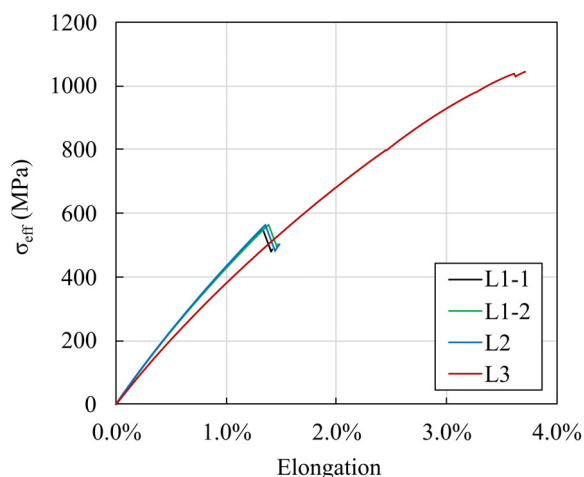er, dynamic crack propagation might have started at anytime between two frames and in such a case, the actual crack speeds would have been greater than our estimation). Such a transition to dynamic crack propagation regime can be explained by the fact that the compressive normal stresses at the interfaces are concentrated only near the drop-off and reduce rapidly towards the thick end, while the interlaminar shear stresses decrease gradually as discussed in Reference 13.

In the next frame taken 8 μs later at 395 μs, a third delamination initiates at the bottom of the first resin pocket and propagates towards the thin end of the tapered region, where tensile interlaminar normal stresses are dominant. At 403 μs, this third delamination is observed to propagate rapidly towards the thin end of the tapered beam and the lower bound of the average crack tip speed is estimated to be 645 m/s. In the remaining frames, lifting up of the belt sublaminate is followed by the opening of the crack surfaces, especially on the thin side. Such opening behavior can be interpreted as an indicator of a Mode-I dominant crack propagation inside the thin region. This behavior, in fact, is the result of the lifting up of the belt due to the tensile pulling from the right end. The lifting up can also be attributed to the relaxation of the belt sublaminate which is geometrically constrained to a cornered taper shape during manufacturing. It is notable that the residue of the first resin pocket which remains between the two transverse cracks is observed to be still bonded to the core sublaminate, indicating no interaction between the lower-left and the right-handed delaminations.

Micrographs presented in Figure 6 show the postmortem damage pattern in specimen L1-1. In the upper micrograph showing the whole tapered region, it is seen that major delaminations exist between any two of the core, belt, and drop-off sublaminates within and beyond the transition region. Besides these major delaminations, which were also observed clearly in in situ images, one can also distinguish that short delaminations facing towards the thick side exist at bottom-left corners of the second and third resin pockets. Additionally, it is notable that there are straight transverse cracks within the resin pockets rather than or in addition to separations at resin pocket walls. These might have occurred due to a manufacturing impurity; that is, slightly sliding of the

FIGURE 4 Effective stress versus elongation curves for specimens with L1, L2, and L3 layups.

Specimen	Elongation (%)	σ_{eff} (MPa)	PF_{max} (kN)	% load drop
L1-1	1.33	547.6	44.5	12.4
L1-2	1.38	563.3	45.8	12.2
L2	1.35	561.6	45.8	14.6
L3	3.60	1036.5	83.9	0.7

TABLE 2 Elongation, effective stress, load, and percentage load drop values at failure.

FIGURE 5 Plain high-speed camera images (left) and corresponding failure patterns (rights) showing the in-situ damage sequence in specimen L1-1 with an interframe time of 8 μs. Black arrows indicate the estimated locations of delamination fronts.
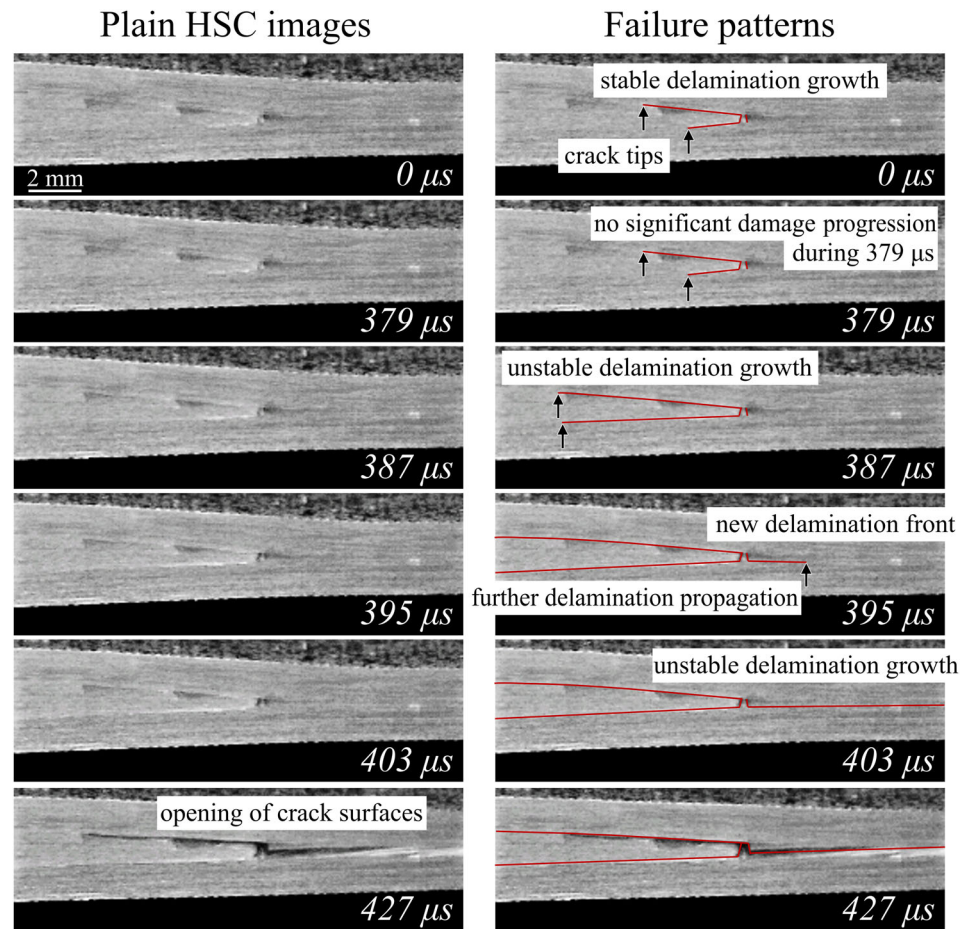
upper drop-off ply over the lower one under longitudinally exerting vacuum pressure.

Detailed investigation of the post-mortem damage can be conducted through micrographs of greater magnification levels. As mentioned earlier for Figure 5, two distinct transverse cracks are seen in the first resin pocket. The right-handed one is a straight transverse crack within the resin pocket, and it is connected to the thin-side delamination. The left-hand side crack, on the other hand, is the separation of cut-ends of dropped-off plies from the resin pocket, hence the junction between the two thick side delaminations. Between these two transverse cracks, there is a residue connected to the core sublaminate, which separates left and right-handed delaminations.

DIC contours of the longitudinal strain ε_y over the tapered face of the beam just before and after the failure are presented in Figure 7A. Before the failure, ε_y distribution is nearly uniform within the thin and thick portions of the beam, and the thin portion is strained more in the axial y-direction as expected. After the failure, on the other hand, ε_y is uniform and at the same level at two ends of the tapered beam. In both cases, ε_y is observed to be nearly uniform in transverse x-direction.
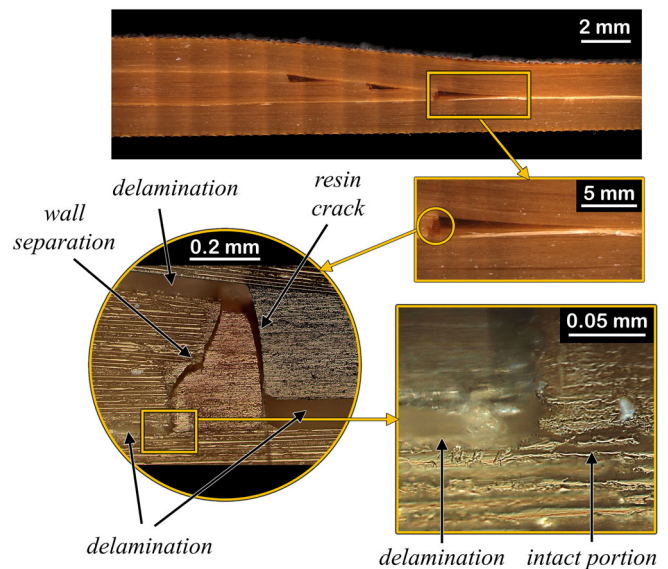

FIGURE 6 Micrographic inspection of the post-mortem damage pattern in specimen L1-1.

In Figure 7B, variation of ε_y along the path AA′ before and after the failure is presented. Before the failure, ε_y is almost constant at far thick and thin ends of the beam
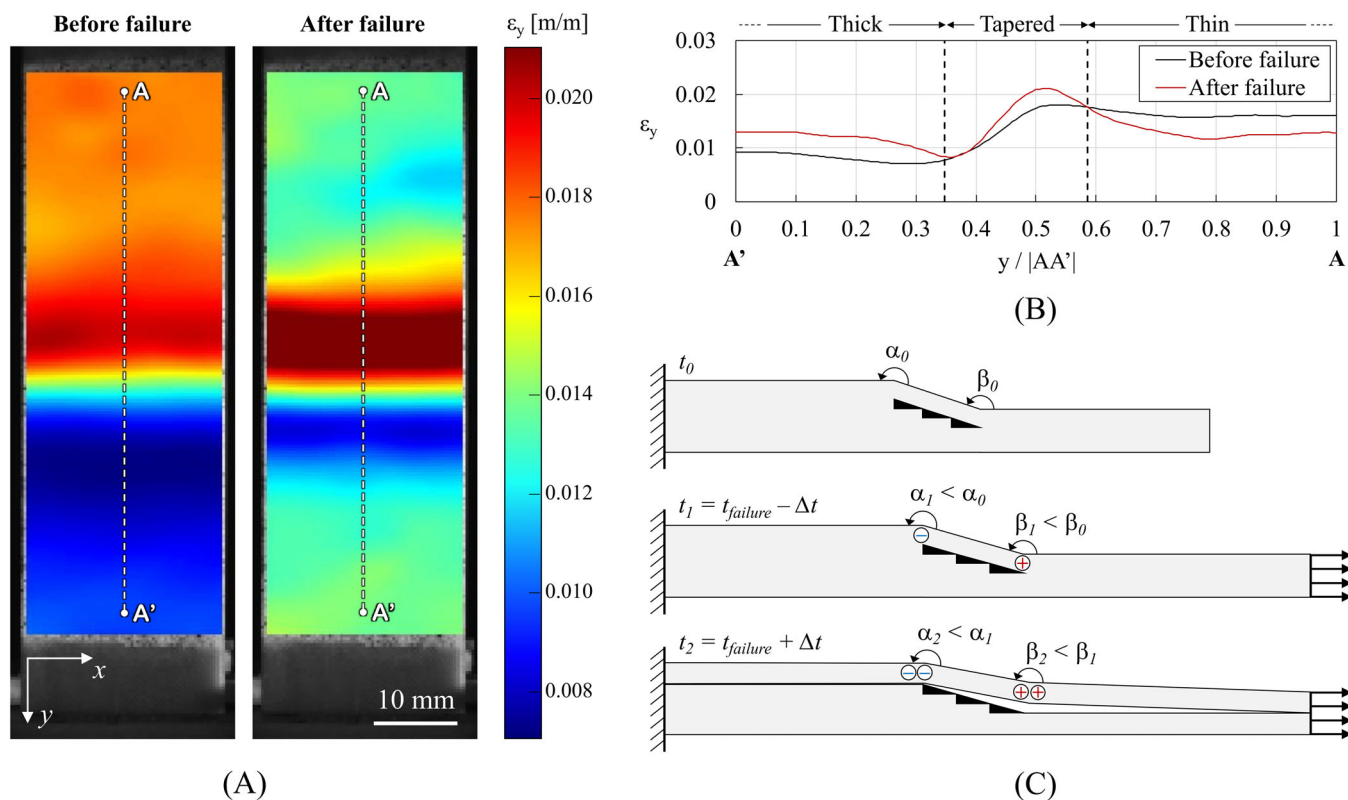
FIGURE 7 (A) DIC contours of ε_y just before and after the failure, (B) variation of ε_y along the path AA′, and (C) schematical illustration of the tapered geometry under tension before and after the failure.

with approximate measured strain values of 0.016 and 0.009, respectively. As it approaches to the tapered region from the thick end, ε_y slightly decreases. Conversely, as it approaches to the tapered region from the thin end, ε_y slightly increases. A smooth transition of ε_y is observed along the tapered region of the beam. After the failure, farfield ε_y values come to a similar level which is about 0.013 strain. Additionally, a plunge and rise in ε_y is observed near the thick and thin boundaries of the tapered region, respectively, which are interconnected by means of a steeper strain transition compared to the no failure case.

The plunges and rises observed in the axial strain beyond the transition region are mainly due to the bending of the belt sublaminate.[18] To understand the physical basis of such a strain variation, it is useful to examine a hypothetical case illustrated in Figure 7C. Consider an asymmetrically tapered beam fixed in the axial direction at its thick end. At time t_0, the beam is load-free, and the angles made by the tapered edge to the flat edges of the thick and thin portions are α_0 and β_0, respectively. When this beam is pulled axially until a time t_1 which corresponds to an instant just before the failure, whole length of the belt sublaminate elongates. Such an elongation results in a change in the angles α and β, such that

$\alpha_1 < \alpha_0$ and $\beta_1 > \beta_0$. Accordingly, compressive and tensile strains are induced by the bending of the corners at the thick and thin transition boundaries, respectively. Assume that further elongation causes the beam to fail only in the form of a full-length delamination underneath the belt sublaminate at a time t_2. Since the belt under tension tends to split up from the core on the thin side, such delamination failure leads to further decrease in α and increase in β. Therefore, splitting of the belt induces higher bending strains at the transition boundaries, which appear as a plunge and a rise in the red curve shown in Figure 7B.

Since in situ observations of specimen L1-1 from the edge were limited to HSC images captured at the load drop, no information is available about the formation and stable growth of the initial delaminations seen in the first frame of Figure 5. Therefore, in the case of the next specimen (L1-2), static photographs have also been taken from the edge during the static tensile loading with an interframe time of 10 s. Furthermore, DIC analysis was conducted to obtain strain fields on the specimen side prior to and during the failure event.

In Figure 8A, images 1–6 show shear strain field contours along the tapered section of the beam during the static loading. Precise locations of images 1–6 are
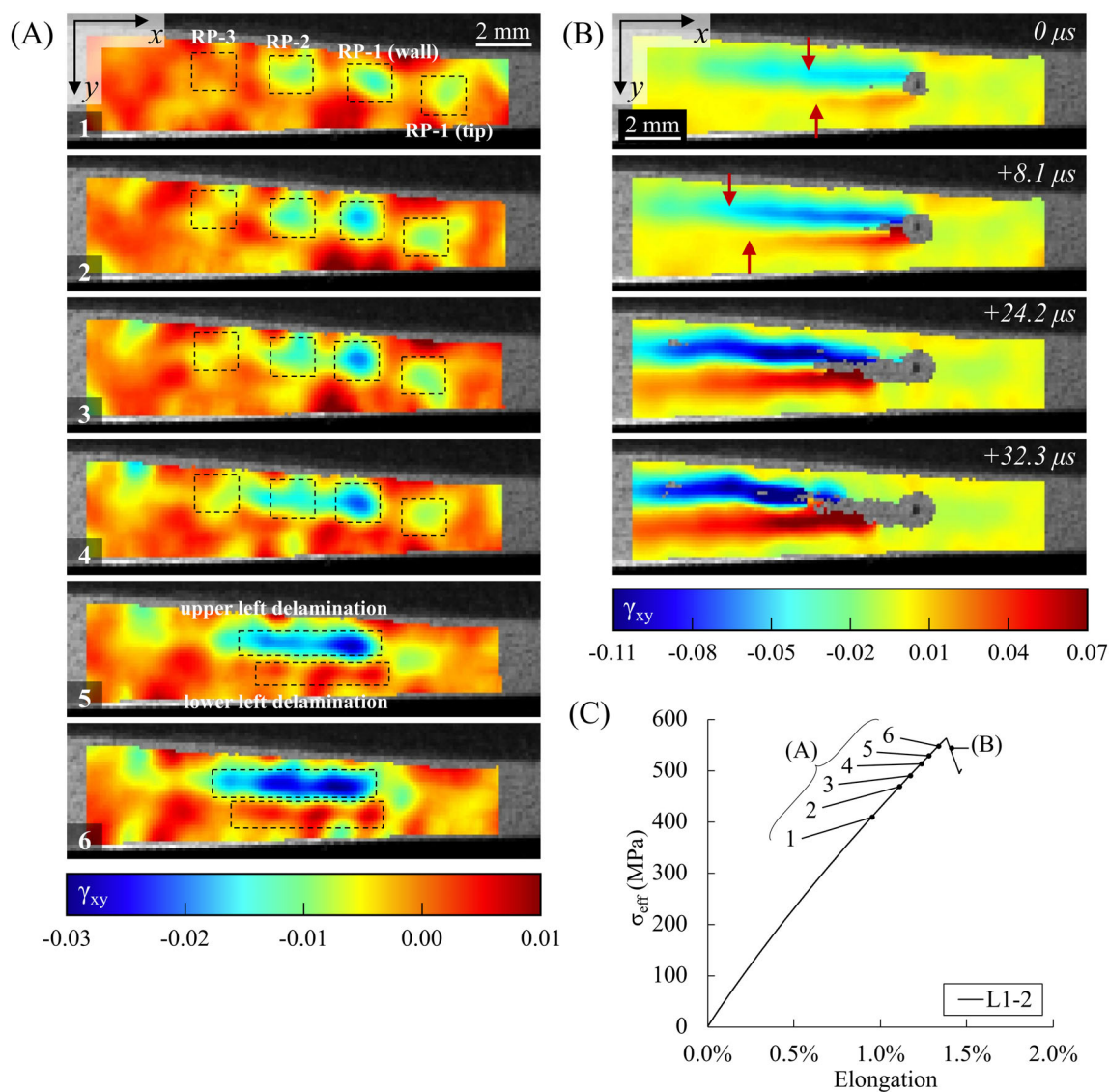
FIGURE 8 Shear strain fields along the tapered section of specimen L1-2 obtained via DIC (A) during static loading and (B) during dynamic failure with the images taken at the corresponding points on the effective stress versus elongation curve shown in (C). Red arrows in (B) indicate the estimated locations of delamination fronts.

indicated on the force–stroke curve of specimen L1-2. Although there is a single load drop at the end of the force–stroke curve, three shear stress concentrations are observed in image 1 taken at 0.94% elongation. These shear concentration zones correspond to the second drop-off site, the first drop-off site, and the thin end of the first resin pocket from left to right, respectively. The shear strain concentration at the first drop-off is observed to be more dominant in image 2 taken at 1.11% elongation and starts to extend towards the thick side through images 3 and 4, merging with the next concentration at the second drop-off. These observations demonstrate the initiation of failure at the first drop-off site, and then its tendency to propagate towards the thick side along the interface between the belt and resin pockets. In the last two images 5 and 6 taken at 1.27% and 1.33% elongation,

respectively, shear strain is concentrated along the belt – resin pockets interface in a wide continuous form rather than localized concentrations. This indicates that a delamination initiating from the first drop-off propagates stably towards the thick side of the tapered beam at the belt/drop-off interface with no sign in the force–stroke curve.

As seen in the force–stroke curve of L1-2 shown in Figure 8C, failure occurs at 1.36% elongation leading to an almost 12% drop in the tensile load carrying capacity of the tapered beam. A sequence of shear strain fields observed during the dynamic failure is presented in Figure 8B. The last frame of the HSC image sequence before the failure propagation is taken as the reference frame and denoted by 0 μs in Figure 8B. In this frame, two interface cracks are recognized through the high

absolute shear strain regions depicted by blue and red colors. In the next frame taken at 8.1 µs, upper and lower delaminations propagate towards the thick section with lower bound average tip speeds of 347 and 297 m/s, respectively. As mentioned earlier, the crack speed estimations here represent the lower bound of delamination growth rates and these values are at similar order of magnitude with those measured at the failure of L1-1. Both cracks complete their dynamic travel in the tapered region and reach the thick side of the beam at 32.3 µs. Unlike the sequence observed in specimen L1-1, no delamination initiates at the tip of the first resin pocket towards the thin side of specimen L1-2. However, the nucleation of two initially stable delaminations from the 1st resin pocket towards the thick side, followed by their subsequent unstable growth, has been consistently observed in both L1 specimens, thereby affirming the dynamic failure sequence in this configuration.

3.3 | Results of L2 configuration

HSC images of the failure sequence observed in specimen L2 are presented in Figure 9. The left-hand side set of images depicts the raw display of high-speed frames, and the right-hand side set illustrates the failure pattern through red lines on the same high-speed frame. The first image in Figure 9 is the last frame captured by the camera just before initiation of the dynamic failure. The time of this image is taken as the reference time and denoted by 0 µs. In this reference image, transverse crack formations can be observed at the first four drop-off sites. From the history of HSC images, it is depicted that the transverse cracks at the 2nd, 3rd, and 4th drop-off sites occurred inside the last second before the initiation of dynamic failure. On the other hand, the transverse crack at the first drop-off site was noticeable even in the first HSC frame, indicating that this crack might have occurred at any time during the static loading. One important observation about the tensile failure sequence in specimen L2 is that no stable delamination propagation occurs during the static loading in contrast to L1 configuration.

Dynamic delamination sequence in specimen L2 is presented through the images 2–5 in Figure 9 with an interframe time of 8.1 µs. 8.1 µs after the reference frame, two delaminations initiate from the transverse crack at the first drop-off site and propagate towards the thick side of the beam at the upper and lower interfaces of the drop-off sublaminate, respectively. At this instant, the length of the upper delamination is approximately three times greater than the lower delamination. Therefore, it is presumable that the upper delamination initiated in the first place. Using the estimated crack tip positions,

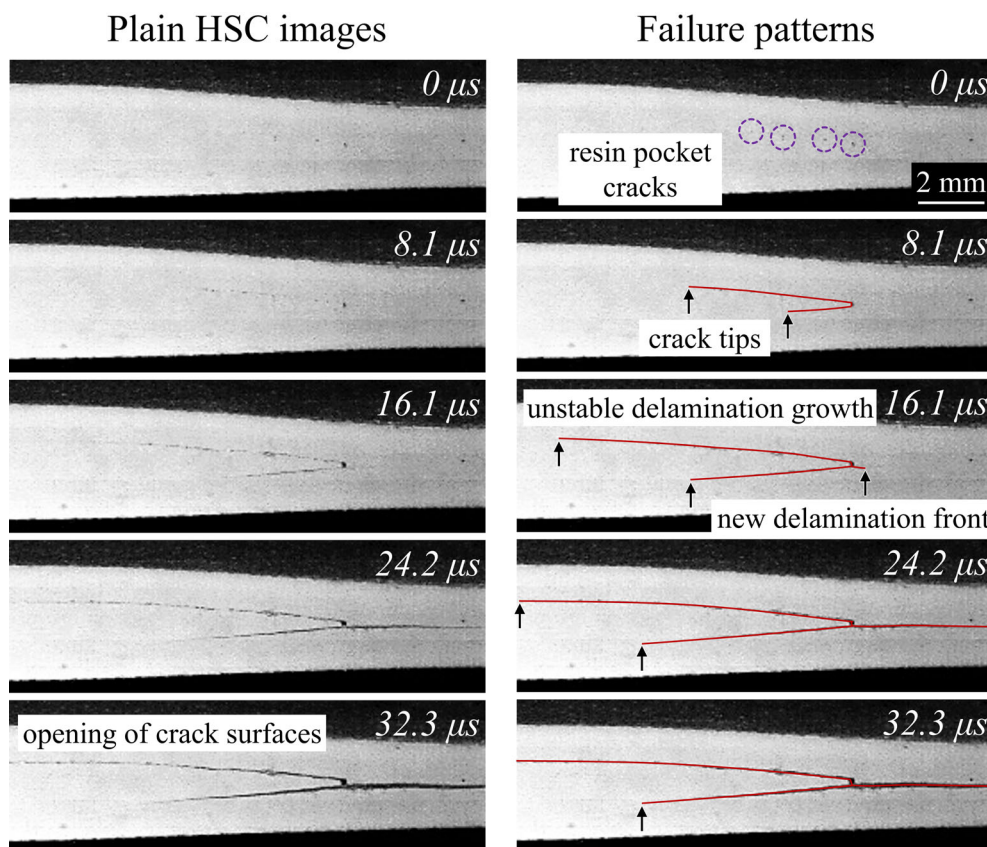**Plain HSC images** / **Failure patterns**

FIGURE 9 Plain high-speed camera images (left) and corresponding failure patterns (right) showing the dynamic failure sequence in specimen L2. Black arrows indicate the estimated locations of delamination fronts.

lower bound values of average tip speeds of upper and lower left delaminations between 0 and 8.1 μs can be calculated as 608 and 237 m/s, respectively. At 16.1 μs, further propagations of the upper and lower left-hand delaminations are observed with average speeds of 495 and 366 m/s, respectively. Meanwhile, a third delamination facing towards the thin side of the tapered beam originates from the bottom end of the transverse crack at the first drop-off site. In the last two HSC images taken at 24.2 and 32.3 μs, further propagations of these delaminations followed by the opening of the crack surfaces can be observed. The lower bound estimation of the average tip speed of the third delamination between 16.1 and 24.2 μs is calculated as 480 m/s.

Figure 10 depicts the post-mortem failure pattern in specimen L2 via a tiled micrograph of the tapered region in conjunction with close-up micrographs of all six resin pockets (after white paint has been removed). In these micrographs, the residual opening of the delaminated surfaces can be clearly observed. Besides, the microscopic inspection of the resin pockets reveals that transverse cracks exist also at the 5th and 6th drop-off sites which were not visible in the HSC images. It is clearly seen that all these transverse cracks are separations at resin pocket walls rather than independent cracks within resin pockets such as ones observed in the staircased/grouped unidirectional configuration L1. This observation supports our claim which was the manufacturing impurity in grouped drop-offs causing transverse cracks within resin pockets (see the discussion of Figure 6).

The overall mechanical behavior of specimen L2 is highly similar to that of the other unidirectional configuration L1 in terms of the load–displacement response, damage sequence and pattern, and crack tip speeds except for a few minor differences. In both drop-off configurations, the initial damage occurs as a transverse crack at the first drop-off site, that is, the vertical wall of

the closest resin pocket to the thin end of the tapered region. Then, major delaminations branch from this transverse crack in the following order and propagates through (i) the belt-dropped plies interface, (ii) the core-dropped plies interface, and (iii) the belt-core interface (not always). Furthermore, lower bounds of crack tip speeds at initiation are measured to be ranging from 230 to 650 m/s in both cases. At this point, it is worth reminding that L1 and L2 are staircased-grouped tapered configurations but L1 configuration has a total of three drop-off sites with two ply drop-offs at each one while L2 configuration has a total of six drop-off sites with single ply drop-off at each.

One of the minor differences between the mechanical behaviors of L1 and L2 configurations is the propagation rates of delaminations. An initially stable delamination propagation occurs during the static tensile loading of L1 specimens but not that of L2 specimen. Although such delamination propagation makes no change in the load–displacement curve, that is, does not affect the tensile load carrying capacity of the tapered beam, further propagation of these cracks, for example, under cyclic bending loading might pose a risk for the structural integrity. However, damage tolerance of asymmetrically tapered beams is beyond the scope of this paper and further investigation should be conducted to clarify this issue. To conclude, the damage evolution sequence in tensile loaded staircased-grouped tapered beams having unidirectional layup is found to be independent of the number of drop-off sites, or in other saying, of the number of dropped plies at each of these sites.

3.4 | Results of L3 configuration

HSC images illustrating the dynamic failure sequence observed in specimen L3 and corresponding failure
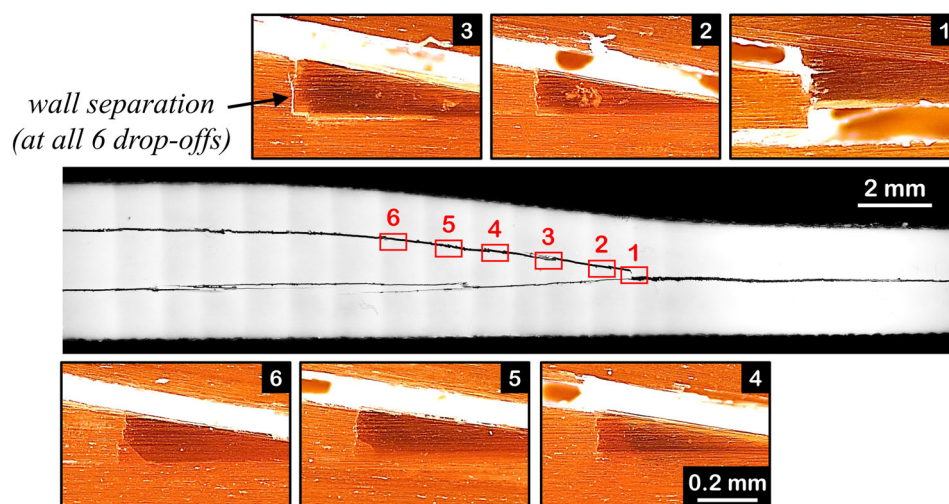

wall separation (at all 6 drop-offs)

FIGURE 10 Micrograph showing the post-mortem damage pattern in specimen L2.

patterns are presented in Figure 11. On the monitored edge of the specimen, three thin black lines are transversely drawn in order to facilitate the detection of any delamination which may propagate to the thick end of the tapered region. The first frame of Figure 11 is the last frame captured before the initiation of dynamic delamination cracks and denoted by 0 μs. In this frame, two consecutive transverse cracks are observed in the vicinity of the first drop-off location. Snapshots taken during the static loading with equal interframe times reveal that these left and right-hand transverse cracks appear at 1.84% and 2.62% elongation, respectively. In contrast to the observations made for the L1 configuration, these transverse cracks do not induce any stable delamination until a sudden failure occurs at 3.60% elongation.

Dynamic delamination sequence in specimen L3 is presented through the last three images in Figure 11 with an interframe time of 8.1 μs. At 8.1 μs, two delaminations are observed to initiate from the existing transverse cracks at the first drop-off. The left delamination is facing the thick side and propagating at the interface of belt and drop-off sublaminates while the right delamination is facing the thin side and propagating at the belt/core interface. Regarding the length of these two delaminations at 8.1 μs, it is deduced that the right-hand delamination initiates earlier. Following its initiation, the right-hand side delamination facilitates lifting-up of the belt sublaminate under tension and leads to higher normal stresses along the belt/drop-off interface starting from the first drop-off site. Consequently, the second delamination occurs at the belt/drop-off interface in the form of an opening crack, as

seen more clearly in the frame taken at 16.1 μs. It should be noted that the shear stresses at this interface is considerably smaller in this configuration than those emerging in the unidirectional L1 and L2 configurations since a more compliant drop-off sublaminate is obtained by the use of ±45° oriented plies. This fact brings about two important outcomes: (i) relatively lower interlaminar shear stress values prevent early formation of delamination facing the thick side at the belt/drop-off interface, and (ii) delamination occurs on the thin side when interlaminar normal stresses reach to maximum allowable values at relatively higher loads. The latter outcome explains the fact that specimen L3 fails at 83.9 kN while unidirectional configurations fail in the range of 44–46 kN.

At 16.1 μs, the two former delaminations propagate further, a third delamination initiates at the first drop-off site and propagates towards the thick side at the core/drop-off interface. One possible mechanism triggering this delamination can be the through-the-thickness travel of stress waves generated by the formation of an opening crack at a parallel interface. In such a scenario, the third delamination initiates from the bottom end of the transverse crack at the first drop-off where a high stress concentration is pristine due to the existence of a crack tip. The HSC image taken at 16.1 μs also reveals the existence of a short interface crack between two plies in the drop-off sublaminate. This short interface crack is connected to the belt/drop-off interface with two transverse cracks from its two ends. Together with the fact that the aforementioned cracks do not appear in the first two frames, these observations may indicate that such cracks are
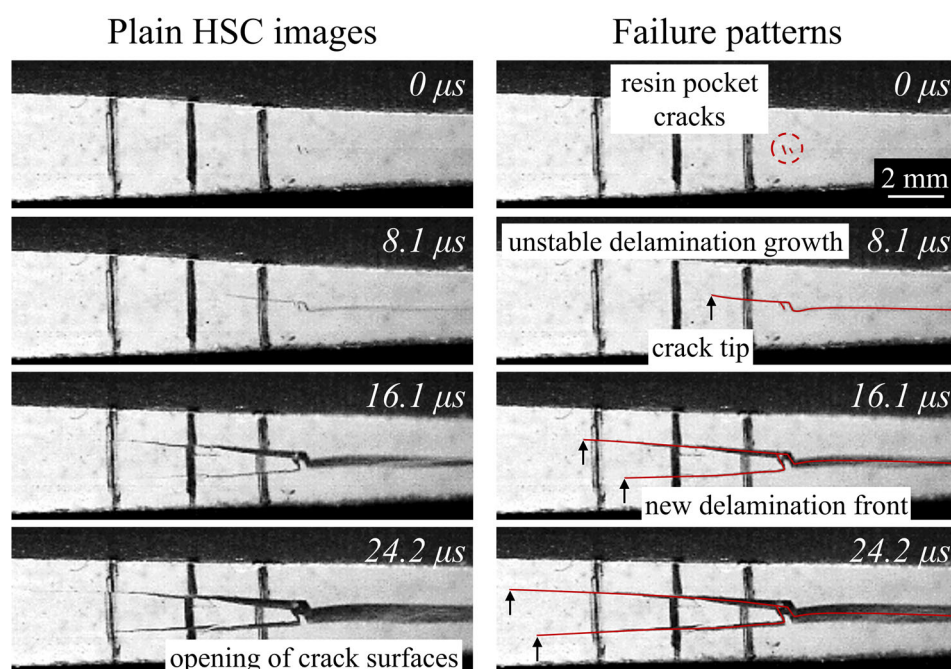
Plain HSC images   Failure patterns

FIGURE 11 Plain high-speed camera images (left) and corresponding failure patterns (right) showing the dynamic failure sequence in specimen L3. Black arrows indicate the estimated locations of delamination fronts.
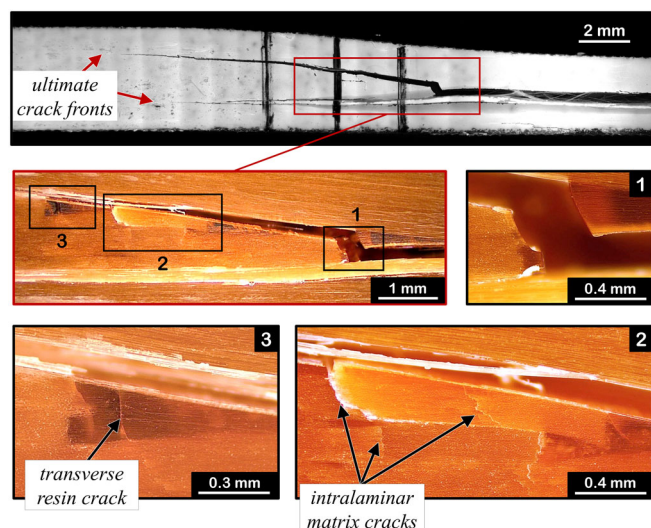
FIGURE 12 Post-mortem micrographs of specimen L3 showing three major delaminations together with ply and resin cracks.

TABLE 3 Estimated delamination crack tip speeds measured from successive HSC frames.

	Crack tip speeds		
Specimen	**Upper delamination on the thick side**	**Lower delamination on the thick side**	**Delamination on the thin side**
L1-1	$\geq$389 m/s[a]	$\geq$584 m/s[a]	$\geq$645 m/s[b]
L1-2	$\geq$347 m/s[a]	$\geq$297 m/s[a]	N/A
L2	$\geq$608[a], 495 m/s	$\geq$237[a], 366 m/s	$\geq$480 m/s[b]
L3	$\geq$304[a], 563, 325 m/s	$\geq$702[a], 385 m/s	$\geq$729 m/s[b]

Note: Greater and equal symbol indicates the lower bound of the average tip speed. Multiple values are reported wherever measurement is possible.
[a]The exact initiation time is unknown and can be anytime between two HSC frames.
[b](i) The exact initiation time is unknown and can be anytime between two HSC frames, and (ii) the crack tip reaches out of bounds of the second HSC frame.

formed during the propagation of the upper delamination. In the last frame of Figure 11 captured at 24.2 μs, further propagation of the delaminations and opening of the crack surfaces can be observed.

Based on the estimated locations of delamination fronts at 8.1 μs, lower bounds of average crack tip speeds at initiation are calculated as 304 and 729 m/s for upper-left- and right-hand sided delaminations, respectively. Between 8.1 and 16.1 μs, the average crack tip speed of the upper-left delamination is measured as 563 m/s and the lower bound average crack tip speed of lower-left delamination is calculated as 702 m/s. Between 16.1 and 24.2 μs, the average crack tip speeds of the upper-left and lower-left delaminations are measured to be 325 and 385 m/s, respectively, which reveals decreasing delamination growth rate beyond the thick side of the transition region.

Figure 12 illustrates the post-mortem damage patterns in specimen L3 via a tiled micrograph of the tapered region in conjunction with the close-up micrographs of the three drop-off locations. It is clearly seen that both thick side delaminations are arrested a few millimeters after leaving the transition region. It has been shown that these delaminations initiate dynamically; however, their regime turning into the stable growth should not be unexpected in presence of high through-the-thickness compressive stresses due to a relatively larger elongation at failure value in L3 configuration.

Transverse cracks within all three resin pockets are noticeable in the post-mortem images of the specimen in Figure 12. In addition to these resin cracks, several matrix and interface cracks can be observed in the vicinity of the second drop-off. These matrix and interface cracks, which are not observed in unidirectional configurations, appear only in this layup configuration where the dropped plies are oriented in $\pm45°$. Such dissimilarity is expected for two reasons: (i) the matrix strength is much less than the fiber strength under both tension and compression, and (ii) a higher interlaminar normal stress accumulation is expected at the belt/drop-off interface of L3 configuration since the failure occurs at a much higher load value. The second reason may be worth to consider when these cracks occur due to through-the-thickness propagation of relaxation waves, which was the proposed mechanism for these follow-up interface and matrix cracks (see the discussion about Figure 11).

4 | DISCUSSION

The unstable delamination growth in asymmetrically tapered beams is characterized quantitatively by the measurements of lower bounds of average crack tip speeds for the first time to the best of our knowledge. This unique crack tip speed data, presented in Table 3, proves that failure occurs dynamically in all tested configurations, where lower bounds of delamination tip speeds at initiation range between 230 and 730 m/s. The fact that measured values are lower bounds and average between two successive images implies that the instantaneous actual crack tip speed following the onset of the unstable growth can be considerably higher than estimated.

When the average crack tip speeds of all configurations are comparatively evaluated, an intriguing consistency can be observed: the lower bound crack speeds observed in the delamination on the thin side are generally greater than those measured for the two delaminations on the thick side. Although the comparison of lower bounds may raise questions, the observed consistency suggests that it may not be a mere coincidence. Due to the tapered geometry, it is expected that the high delamination growth rates would be suppressed by the effect of increasing through-the-thickness compressive (TTC) stresses on the thick side of the transition region, while the tensile stresses on the thin side would not exert a diminishing effect on the crack growth rate. This can be regarded as an in situ experimental evidence supportive of the modeling strategy called "through-the-thickness compression enhancement", where the interlaminar shear strength and Mode-II strain energy release rate are defined as a function of local TTC stresses.[15,19]

The great detail in our high-fidelity real-time observations also provides in situ experimental evidence for typical failure mechanisms in tapered laminates proposed by earlier studies which were based on post-mortem observations of traditional tensile experiments and analytical approaches. Regardless of ply dropping methodology, initial failure occurs as a transverse crack at the first drop-off site. In unidirectional configurations, further transverse cracks are observed in other drop-off sites. The sequence of failure in both unidirectional configurations (either one or two discontinuous plies at each drop-off) is characterized by two delaminations nucleating from the initial transverse crack and propagating towards the thicker end of the beam first in a stable and then in an unstable manner. In the third configuration with a $\pm 45°$ ply drop-off sublaminate, the higher compliance of $\pm 45°$ drop-off layers reduces stress concentrations at ply discontinuities, delaying the delamination in the thick section. In contrast to unidirectional configurations, initial delamination occurs in the thin section at higher loads where interlaminar normal stresses reach maximum allowable values. Accordingly, an improved tensile strength with a minor loss in stiffness can be achieved by having a $\pm 45°$ drop-off sublaminate rather than a 0° unidirectional layup.

The use of $\pm 45°$ oriented plies as drop-off layers results in a more compliant drop-off sublaminate and increases the damage resistance of the tapered beam. Such a laminate design delays the failure of the tapered beam compared to unidirectional layups but causes through-the-thickness compressive stresses acting on drop-off plies to increase further. These high through-the-thickness stresses suppress the growth rate of dynamic delaminations surrounding the drop-off

sublaminate, which in turn results in crack arrest a few millimeters after reaching the thick region.

5 | CONCLUSIONS

In this article, the dynamic failure process in asymmetrically tapered beams under tensile loading has been studied experimentally. Staircased-grouped type tapered GFRP laminates were manufactured featuring three different layups: $[0_6/(0_2)_3/0_6]$, $[0_6/\underline{0_6}/0_6]$, and $[0_6/(\pm 45)_3/0_6]$. Static tensile experiments were conducted, and real-time observations of the dynamic failure sequence were performed via high-speed camera (HSC) images captured at 124,000 fps. DIC analyses were performed on the tapered face and edge of the beam to justify the failure mechanisms observed in HSC images. In situ real-time experimental evidence of the dynamic failure sequence in staircased-grouped type tapered laminates under tensile loading was presented. Quantitative characterization of unstable delamination growth was performed by measurement of lower bounds of average crack tip speeds.

Several key conclusions can be drawn from this study. First, we show that the failure process in staircased/grouped asymmetrically tapered beams tends to be dynamic, with measured lower bound values of delamination tip speeds within the range of 230–730 m/s. Moreover, estimations of the delamination growth rate on the thin side, where tip speeds faster than 600 m/s were recorded, consistently surpassed those of the two delaminations on the thick side. This disparity is attributed to the high compressive through-the-thickness stresses acting on the drop-off sublaminate.

In 0° unidirectional configurations, we observed that unstable growth of delaminations initiates within the tapered region and continues along both thick and thin ends of the beam. The incorporation of $\pm 45°$ plies in drop-off sublaminate proved to delay the failure of the tapered beam due to the compliant layers, thereby causing through-the-thickness compressive stresses to increase further and resulting in crack arrest slightly after reaching the thick region. Overall, the detailed high-fidelity real-time observations provides in situ experimental evidence that supports earlier findings regarding the failure mechanisms of tapered laminates, which were previously proposed based on post-mortem observations made or analytical approaches.

As a final note, we believe that the idealized drop-off configurations in tapered laminates provide clear visualization of the failure sequence consisting of a resin pocket failure followed by dynamic delamination growth. We

propose that the intricate sequence and patterns of dynamic failure presented in this paper can serve as a comprehensive benchmark to assess the accuracy of finite element predictions of the failure of tapered laminates, particularly those involving interface fracture models with a cohesive formulation or the virtual crack closure technique. A demonstration of such assessment is made in the follow-up computational study of this experimental research,[20] where excellent agreement is shown between the high-fidelity finite element simulations and our in situ real-time experimental observations.

ACKNOWLEDGMENTS

DATA AVAILABILITY STATEMENT

Data will be made available on request.

REFERENCES

1. Armanios EA, Parnas L. Delamination analysis of tapered laminated composites under tensile loading. In: O'Brien TK, ed. *Composite Materials: Fatigue and Fracture*. Vol 3. ASTM International; 1991; 340-340-19:chap Stp17726s.
2. Hoa SV, Daoust J, Du BL, Vu-Khanh T. Interlaminar stresses in tapered laminates. *Polym Compos*. 1988;9(5):337-344. doi:10.1002/pc.750090506
3. Curry JM, Johnson ER, Starnes JH. Effect of dropped plies on the strength of graphite-epoxy laminates. *AIAA J*. 1992;30(2):449-456. doi:10.2514/3.10938
4. Fish JC, Lee SW. Delamination of tapered composite structures. *Eng Fract Mech*. 1989;34(1):43-54. doi:10.1016/0013-7944(89)90241-5
5. Fish JC, Vizzini AJ. Tailoring concepts for improved structural performance of rotorcraft flexbeams. *Compos B Eng*. 1992;2(5):303-312. doi:10.1016/0961-9526(92)90028-5
6. Cui W, Wisnom MR, Jones M. Effect of step spacing on delamination of tapered laminates. *Compos Sci Technol*. 1994;52(1):39-46. doi:10.1016/0266-3538(94)90006-X
7. Wisnom MR, Jones MI, Cui WC. Failure of tapered composites under static and fatigue tension loading. *AIAA J*. 1995;33(5):911-918. doi:10.2514/3.12510
8. Wisnom MR, Dixon R, Hill G. Delamination in asymmetrically tapered composites loaded in tension. *Compos Struct*. 1996;35(3):309-322. doi:10.1016/0263-8223(96)00044-X
9. Vidyashankar BR, Krishna Murty AV. Analysis of laminates with ply drops. *Compos Sci Technol*. 2001;61(5):749-758. doi:10.1016/S0266-3538(01)00010-0
10. Wisnom MR. Delamination in tapered unidirectional glass fibre-epoxy under static tension loading. *Presented at: 32nd Structures, Structural Dynamics, and Materials Conference*; 1991. doi:10.2514/6.1991-1142
11. Allegri G, Wisnom MR, Hallett SR. A simplified approach to the damage tolerance design of asymmetric tapered laminates. Part I: methodology development. *Compos Part A Appl Sci Manuf*. 2010;41(10):1388-1394. doi:10.1016/j.compositesa.2010.05.009
12. Gan KW, Allegri G, Hallett SR. A simplified layered beam approach for predicting ply drop delamination in thick composite laminates. *Mater Des*. 2016;108:570-580. doi:10.1016/j.matdes.2016.06.105
13. Mukherjee A, Varughese B. Design guidelines for ply drop-off in laminated composite structures. *Compos B Eng*. 2001;32(2):153-164. doi:10.1016/S1359-8368(00)00038-X
14. Mukherjee A, Varughese B. Development of a specialised finite element for the analysis of composite structures with ply drop-off. *Compos Struct*. 1999;46(1):1-16. doi:10.1016/S0263-8223(99)00013-6
15. Zhang B, Kawashita LF, Jones MI, Lander JK, Hallett SR. An experimental and numerical investigation into damage mechanisms in tapered laminates under tensile loading. *Compos Part A Appl Sci Manuf*. 2020;133:105862. doi:10.1016/j.compositesa.2020.105862
16. Gordon T, Xu X, Kawashita L, Wisnom MR, Hallett SR, Kim BC. Delamination suppression in tapered unidirectional laminates with multiple ply drops using a tape scarfing technique. *Compos Part A Appl Sci Manuf*. 2021;150:106627. doi:10.1016/j.compositesa.2021.106627
17. Blaber J, Adair B, Antoniou A. Ncorr: open-source 2D digital image correlation Matlab software. *Exp Mech*. 2015;55(6):1105-1122. doi:10.1007/s11340-015-0009-1
18. Kemp B, Johnson E. Response and failure analysis of a graphite-epoxy laminate containing terminating internal plies. *Presented at: 26th Structures, Structural Dynamics, and Materials Conference*; 1985.
19. Gan KW, Hallett SR, Wisnom MR. Measurement and modelling of interlaminar shear strength enhancement under moderate through-thickness compression. *Compos Part A Appl Sci Manuf*. 2013;49:18-25. doi:10.1016/j.compositesa.2013.02.004
20. Dashatan SH, Parnas L, Coker D, Bozkurt MO, Ozen EB. In-situ observation and numerical study of dynamic delamination in tapered composite laminates. *Compos Struct*. 2023;312:116841. doi:10.1016/j.compstruct.2023.116841

How to cite this article: Bozkurt MO, Ozen EB, Yavuz BO, Parnas L, Coker D. High-speed observation of dynamic delamination failure in tapered composite laminates under tensile loading. *Polym Compos*. 2024;1-15. doi:10.1002/pc.28402